Signatures of a topological phase transition in a planar Josephson junction

A. Banerjee, O. Lesser, M. A. Rahman, H.-R. Wang, M.-R. Li, A. Kringhøj, A. M. Whiticar, A. C. C. Drachmann, C. Thomas, T. Wang, M. J. Manfra, E. Berg, Y. Oreg, Ady Stern, and C. M. Marcus

Phys. Rev. B **107**, 245304 — Published 22 June 2023

DOI: 10.1103/PhysRevB.107.245304

Signatures of a topological phase transition in a planar Josephson junction

A. Banerjee,[1] O. Lesser,[2] M. A. Rahman,[1] H.-R. Wang,[2,3] M.-R. Li,[2,3]
A. Kringhøj,[1] A. M. Whiticar,[1] A. C. C. Drachmann,[1] C. Thomas,[4,5] T. Wang,[4,5]
M. J. Manfra,[4,5,6,7] E. Berg,[2] Y. Oreg,[2] Ady Stern,[2] and C. M. Marcus[1]

[1] *Center for Quantum Devices, Niels Bohr Institute, University of Copenhagen, Universitetsparken 5, 2100 Copenhagen, Denmark*
[2] *Department of Condensed Matter Physics, Weizmann Institute of Science, Rehovot, Israel 76100*
[3] *Department of Physics, Tsinghua University, Beijing 100084, China*
[4] *Department of Physics and Astronomy, Purdue University, West Lafayette, Indiana 47907 USA*
[5] *Birck Nanotechnology Center, Purdue University, West Lafayette, Indiana 47907 USA*
[6] *School of Materials Engineering, Purdue University, West Lafayette, Indiana 47907 USA*
[7] *School of Electrical and Computer Engineering, Purdue University, West Lafayette, Indiana 47907 USA*

A growing body of work suggests that planar Josephson junctions fabricated using superconducting hybrid materials provide a highly controllable route toward one-dimensional topological superconductivity. Among the experimental controls are in-plane magnetic field, phase difference across the junction, and carrier density set by electrostatic gate voltages. Here, we investigate wide planar Josephson junctions based on an epitaxial InAs/Al heterostructure, embedded in a superconducting loop, probed with integrated quantum point contacts (QPCs) at both ends of the junction. For a large range of gate voltages, a closing and reopening of the superconducting gap is observed that appears strongly correlated at the two ends of the junction. The reopening occurred roughly at in-plane magnetic field $B_\parallel \simeq 0.2$ T, was uniform across multiple devices, and tunable with phase bias. A narrower range of the junction gate voltage, covering roughly 10% of the operable gate space, supports a zero-bias conductance peak (ZBCP) that appears upon reopening of the gap. However, the height, shape, and even presence of ZBCPs typically differed between the ends, suggesting weak end-to-end correlation. Theoretical modeling suggests an orbital-effect driven mechanism for the gap-reopening. Within this model, the gap reopening represents a topological phase transition when associated with a zero-energy state. While several features of the experimental data are captured by our model, the lack of end-to-end correlation of ZBCPs in the experiment suggests the absence of an uninterrupted topological phase along the junction, presumably due to disorder. Deliberately tuned local end dots show distinctly different phenomenology, particularly with respect to phase bias, providing a check on possible topological and non-topological interpretations.

I. INTRODUCTION

Planar superconductor-normal-superconductor (SNS) Josephson junctions (JJs) with sufficient spin-orbit coupling can exhibit one-dimensional topological superconductivity in the presence of a magnetic field applied parallel to the SN interfaces. Theoretically, the N region under these conditions acts as a quasi-one-dimensional topological wire bounded by trivial superconducting walls, with Majorana zero modes at its ends [1–3]. Compared to alternative nanowire platforms [4–8], planar JJs have a new experimental knob, the phase difference between bounding trivial superconductors, which can lower the magnetic field required to observe a topological phase transition, as reported in recent experiments in Al/InAs [9, 10], Al/HgTe [11] and NbTiN/InSb [12].

Previous studies on related structures [9] demonstrated the formation of a zero-bias conductance peak (ZBCP) at one end of an Al/InAs planar JJ device. The parallel magnetic field, $B_\parallel$, at which the ZBCP first appeared depended on the phase difference, ϕ, across the junction, first appearing at $\phi \sim \pi$, as expected for a topological phase transition [1, 2]. A related effect was reported by Ren *et al.* [11], who found that the ZBCP appears in a diamond-shaped region in the ϕ–$B_\parallel$ plane. Ke *et al.* observed an expected minimum of critical current at a gate-voltage dependent value of $B_\parallel$ [12]. Dartiailh *et al.* reported a similar signature and additionally detected a π phase shift of the current-phase relation associated with revival of the supercurrent [10].

Here, we investigate topological superconductivity in planar JJs using a device design that helps preserve a hard superconducting gap in wide leads in the presence of $B_\parallel$. This goes beyond our previous investigation of planar JJs [9], where superconducting leads were narrow compared to the superconducting coherence length. In nanowires, or in Josephson junctions with narrow superconductors (nanowire limit), the topological phase has a weak dependence on ϕ, is strongly tuned by the Fermi energy and appears at relatively large values of $B_\parallel$ [3]. In contrast, in a junction made of semi-infinite superconductors (Josephson junction limit), topological transitions are tuned primarily by varying ϕ and $B_\parallel$, with weak dependence on the Fermi energy. Additionally, phase-biasing allows the topological phase transition to occur at low values of $B_\parallel$, including at $B_\parallel = 0$ in an ideal junction biased at $\phi \sim \pi$ [1, 2].

Our junctions are embedded in a superconducting loop, allowing controlled biasing of ϕ using externally applied flux, and the junction region can now be probed

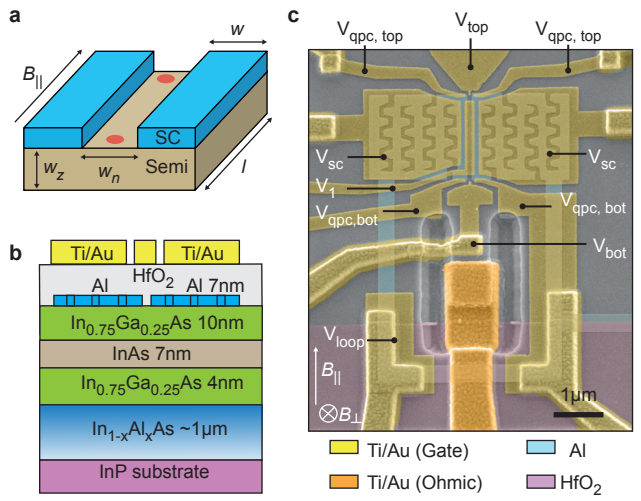

FIG. 1. **Planar Josephson junction device.** (a) Schematic of a planar Josephson junction consisting of two superconducting leads (blue) in epitaxial contact with the underlying semiconductor (brown). Between the leads of width $w = 1.8\,\mu$m was a semiconductor (normal) region of width $w_n = 100$ nm and length $l = 1.6\,\mu$m. The nominal thickness $w_z \sim 20$ nm of the active semiconductor region, where the electron wave-function is expected to be confined, contains two barriers and the InAs quantum well. Red dots schematically indicate the positions of theoretically predicted Majorana zero modes in the topological phase. (b) Schematic cross section shows the Al/InAs heterostructure with layer thicknesses along with dielectric and gate layers. Leads and junction were covered by 15 nm of HfO_2 dielectric deposited by atomic layer deposition and Ti/Au electrostatic gates. (c) False-color electron micrograph of a representative device. The superconducting leads have meandering perforations to allow partial depletion below using gate voltage V_{SC}. Leads are connected by a superconducting loop allowing phase biasing of the junction using a small out-of-plane magnetic field $B_\perp$. Tunnelling spectroscopy is performed using quantum point contacts at the junction ends, controlled by voltages $V_{\rm qpc,top}$ and $V_{\rm top}$ on the top and $V_{\rm qpc,bot}$ and $V_{\rm bot}$ on the bottom. The InAs layer forms the top-end ohmic contact, and a Ti/Au layer forms the bottom-end ohmic contact.

at both ends via tunnelling spectroscopy using quantum point contacts (QPCs). This feature goes beyond previous planar JJ experiments, and is particularly important for testing topological interpretations of our data. In tuned ranges of junction gate voltage, we observe a closing and reopening of the superconducting gap with increasing $B_\parallel$, along with a concurrent appearance of a ZBCP at one or both ends of the junction. The gap reopening and the appearance of a ZBCP both depend on ϕ and remain concurrent when ϕ is modulated by flux. The closing and reopening of the superconducting gap, together with the formation of a ZBCP is a fundamental signature of a topological phase transition, and to the best of our knowledge, never observed before in any platform that can support topological superconductivity, including previous planar Josephson junction experiments. Additionally, the reduction of the field scale for the observation of ZBCPs to $B_\parallel \simeq 0.2$ T, compared to $B_\parallel \simeq 0.6$ T in Ref. [9] reflects that our devices operate closer to the Josephson junction limit.

We investigate a simple model of the system that includes spin-orbit coupling as well as both Zeeman and orbital effects of the in-plane magnetic field. The orbital effect is due to the finite thickness of the Al-InAs heterostructure stack, and was not considered in previous investigations of topological superconductivity in planar JJs. The role of orbital effects in the context of topological superconductivity has been investigated in nanowires [13–15]. Superconducting phase bias controlled topological superconductivity, which is closely related to the orbital effect driven mechanism discussed here, is also emerging as an alternative to Zeeman-driven topological superconductivity, and is aimed at overcoming the unwanted effects of large magnetic fields associated with the latter [16, 17]. For realistic parameters, the model exhibits a topological phase for $\sim 10\%$ of parameter space examined. The model also shows non-topological near-closings of the gap. Topologically trivial situations are also explored, particularly focusing on the possibility of zero-energy states arising from confining potentials near the system edge. We compare theoretical predictions for both topological and non-topological scenarios against experimental data.

II. DEVICE

Planar JJ devices were fabricated using an InAs-based heterostructure grown on an InP wafer, with epitaxial Al as the topmost layer of the heterostructure [see Fig. 1(b)]. $In_{0.75}Ga_{0.25}As$ barriers separate the InAs quantum well from the Al layer above and the $In_{1-x}Al_xAs$ graded buffer below. The heterostructure design is optimized with considerations relevant for topological superconductivity [18]. The $In_{0.75}Ga_{0.25}As$ layer between Al and InAs layers serves as a tunneling barrier. Controlling the tunneling rate between the Al and InAs layers is key to obtaining the desired balance between superconductivity (from Al) and semiconducting properties (from InAs) such as a high spin-orbit coupling and large electron g-factors, necessary for topological superconductivity [19]. The composition of the $In_{0.75}Ga_{0.25}As$ barrier and its thickness (10 nm) were optimized to meet these requirements. Strong superconducting proximity effect arises, even though the barrier is insulating, since the electron wave function has a substantial probability density close to the Al layer, resulting in high superconductor-semiconductor interface transparencies [20]. High quality SNS junctions, with S-N interface transparencies ranging from 0.7 – 0.9, have been reported using similar material systems [21, 22].

The JJ and superconducting loop were fabricated by

a combination of selective wet etching of Al (using Transene D etchant) and deep wet etching of the heterostructure stack to form a mesa and U-shaped trench. A Ti/Au layer contacting a patch of the mesa (with Al removed) serves as a sub-micron internal ohmic contact allowing bottom-end tunnelling spectroscopy through a QPC inside the superconducting loop. Patterned HfO_2 dielectric was deposited using atomic layer deposition (ALD) to allow the Ti/Au layer contacting the internal ohmic contact to pass over the superconducting loop. A second layer of ALD HfO_2 was then deposited on the entire chip followed by patterned deposition of Ti/Au gates to electrostatically control the junction and QPCs. The JJ (width $w_n = 100$ nm, length $l = 1.6\,\mu$m) was covered by a gate above the second ALD layer, energized by gate voltage V_1 relative to the leads to control carrier density and mean free path in the junction [Fig. 1(c)]. Dependence of density and mobility on gate voltage was investigated in a Hall-bar geometry made from the same material, with similar dielectric and top gate (see Supplementary Material Fig. S12 [23]).

The Al layer in the leads (width $w = 1.8\ \mu$m) was etched to form meandering perforations (width $\sim$ 100 nm); related structures were theoretically studied in [24, 25]. These perforations allowed depletion of the semiconductor below and laterally when the gate voltage covering the leads was set to a large negative value, $V_{SC} \sim -3$ V. Depletion in the meanders resulted in an improved hard superconducting gap up to $B_{\|} \sim 0.5$ T as shown in Fig. S2 [23]for tunnelling spectroscopy in a lead-like structure. The measured induced gap at $B_{\|} = 0$ was $\Delta^* \simeq 0.2$ mV, essentially identical to the superconducting gap of thin Al, $\Delta_{Al} \simeq 0.2$ mV, suggesting the high interface transparency between the Al layer and the InAs 2DEG [26, 27]. Other lead designs, such as a uniform array of circular perforations, were explored. These geometries suffered from unwanted phase jumps in the presence of a perpendicular magnetic field, presumably due to flux trapping by the circular perforations. We therefore adopted the meandering geometry which avoids flux trapping, but still allows a relatively spatially uniform superconducting proximity effect in the underlying semiconductor.

The two leads are connected through a superconducting loop (with undepleted electron gas below) with area $\sim$12 μm^2 allowing phase biasing of the junction by the application of a perpendicular magnetic field, $B_{\perp}$. One flux quantum, $\Phi_0 = h/2e$, through the loop corresponds to $B_{\perp} \sim 0.17$ mT, small compared to the field that closes the induced gap under the Al ($B_{\perp} \sim 10$ mT) or that drives the Al normal ($B_{\perp} \sim 40$ mT). Split gates controlled by voltages $V_{qpc,top}$ and $V_{qpc,bot}$ electrostatically define constrictions at the top and bottom of the junction to serve as QPC tunnel barriers. Gate voltages V_{top} and V_{bot}, which control densities in the normal regions outside the QPCs, are typically fixed at $\sim +100$ mV.

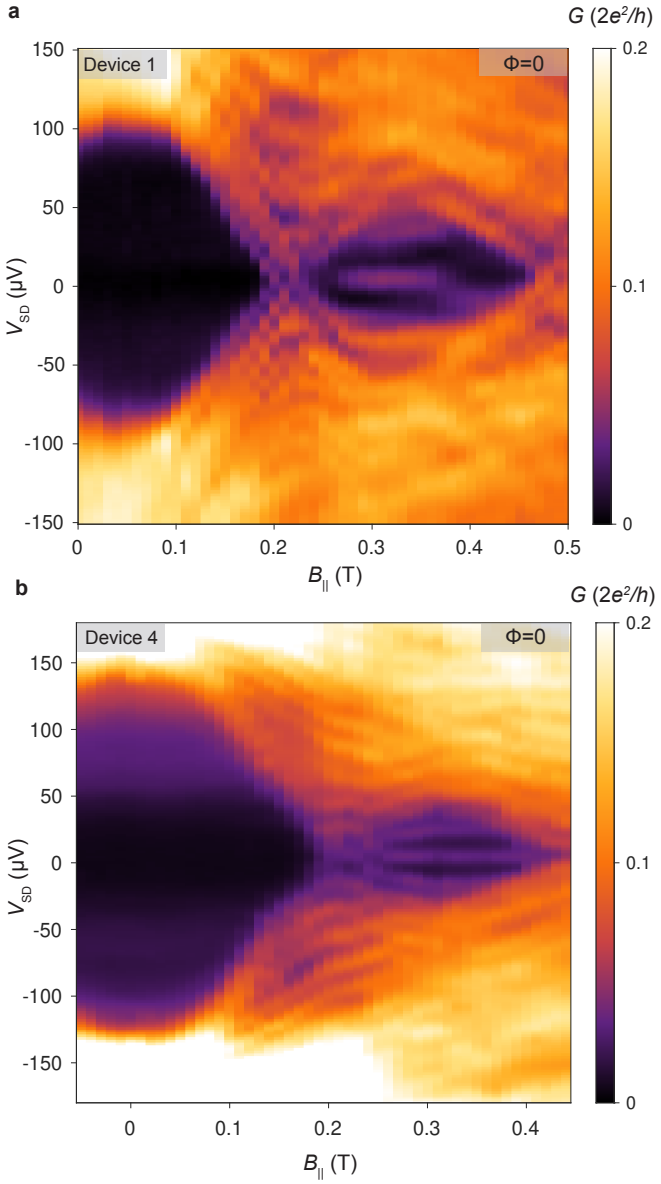

FIG. 2. **Tunnelling spectroscopy as a function of in-plane magnetic field.** Differential conductance, G, as a function of source-drain bias V_{SD} and magnetic field $B_{\|}$ along the junction, showing a closing of the superconducting gap followed by reopening and concurrent appearance of a ZBCP in (a) Device 1, with $V_1 = +86$ mV, $V_{SC} = -1.5$ V, $V_{qpc,top} = -0.31$ V, $V_{qpc,bot} = -3.0$ V, $V_{loop} = -3.0$ V.. (b) Device 4, with $V_1 = +18$ mV, $V_{SC} = -3.5$ V, $V_{qpc,top} = -0.369$ V, $V_{qpc,bot} = -0.352$ V, $V_{loop} = -3.0$ V.

III. RESULTS AND DISCUSSIONS

We first focus on tunnelling spectra at one end of the junction, and then examine spectra measured simultaneously at both ends of the junction. We studied a total of 10 devices of identical design, that showed largely uniform behavior (see Appendix C for a summary).

A. Gap reopening with a zero-bias state

Figure 2 shows differential conductance, G, as a function of source-drain bias $V_{\rm SD}$ measured at the top of the junction (outside the loop) as a function of $B_\parallel$ applied along the junction for two devices. To compensate spurious flux through the superconducting loop due to sample misalignment, G was measured as a function of $B_\perp$ at each value of $B_\parallel$ and reconstructed to plot the $B_\parallel$ dependence at fixed flux (see Methods). Figure 2 is for the case of zero flux, $\Phi = 0$. Top QPC gates were tuned to operate in the tunnelling regime, where G is roughly proportional to the local density of states (see [28], Sec. 11.5).

In Device 1, at $B_\parallel = 0$, we measured a gap $\Delta \sim 80\ \mu$eV, which increased to $\Delta \sim 100\ \mu$eV at $B_\parallel \sim 0.05$ T. Above 0.1 T, a dense but discrete set of tunnelling peaks approach zero bias, closing at $B_\parallel \sim 0.2$ T. With further increase of field, the gap reopened, and a ZBCP appeared, separated from the gapped states. A maximum gap of $\sim 20-30\ \mu$eV was observed in the reopened state before it closed again at $B_\parallel \sim 0.5$ T. In both devices, gap-reopening occurred at $B_\parallel \sim 0.2$ T, and the reopened gap was of similar magnitude.

Focusing on the structure of the ZBCP, we observe ideal ZBCP behavior in Device 4 that remains stuck until the gap closes [Fig. 2(b)]. Deviations from ideal ZBCP behavior are also observed. For instance, in Device 1, the ZBCP begins to deviate from zero bias and splits for $B_\parallel \simeq 0.4$ T[Fig. 2(a)]. The splitting of the ZBCP, both its magnitude and the value of magnetic field where it occurs, is influenced by the phase bias ϕ (Fig. S4 [23]) and the chemical potential (Fig. S6 [23]). Furthermore, we note that the split peaks sometimes show asymmetric tunneling conductance amplitudes. Similar behavior is also seen in Device 2 (Fig. S5 and Fig. S7 [23]).

To aid understanding, we first investigate a disorder-free theoretical model that extends the models developed in Refs. [1, 2]. The proximity-coupled semiconductor is treated as a parabolic band, approximated within a tight-binding model, with effective mass of $m^* = 0.026\, m_e$, where m_e is the free electron mass, and Rashba spin-orbit coupling $\alpha = 15$ meV nm. The superconducting leads are represented by a pairing potential $\Delta \sim 140\ \mu$eV. The in-plane field $B_\parallel$ induces both a Zeeman coupling and an orbital effect. The Zeeman coupling is characterized by an energy scale $E_{\rm Z} = g_{\rm S(N)}\mu_{\rm B}B_\parallel/2$, where $\mu_{\rm B}$ is the Bohr magneton, with g-factors $g_{\rm N} = -8$ in the junction and $g_{\rm S} = -4$ in the leads, based on literature values [29, 30]. The orbital effect is due to the finite cross section of the device, $\gamma w_z(w_n + 2w) \sim \Phi_0/0.2$ T, where $\gamma = 0.4$ is a phenomenological parameter obtained from the leads spectroscopy (see Fig. S2 [23]). As discussed below, this orbital field scale ($\sim$0.2 T) emerges naturally in the model and is not put in by hand. The orbital effect is included by considering a bilayer structure with complex hopping between layers [31] and a linearly increasing superconducting phase difference between the layers and across the junction (see [28], Sec. 6.4 and [32], Sec. 2.9).

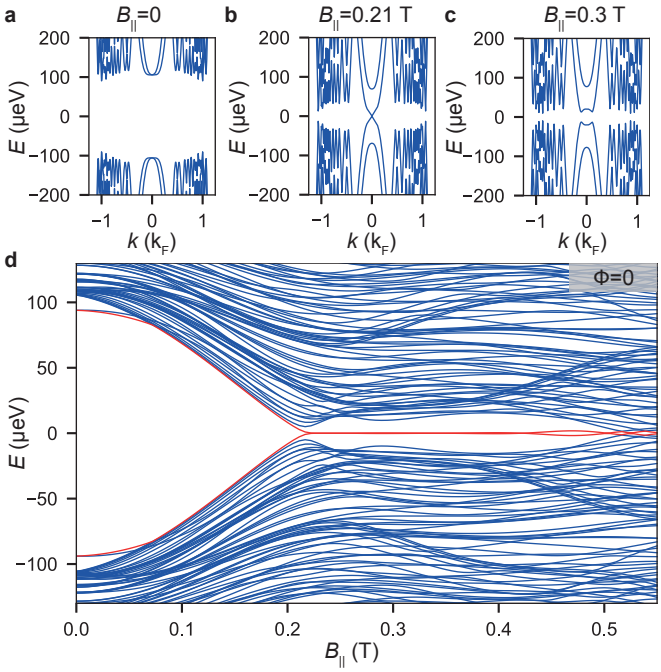

FIG. 3. **Theoretical model of topological phase transition.** Dispersion of the Andreev bound states in a Josephson junction with periodic boundary conditions as a function of momentum k along the junction, parallel to the S-N interfaces (measured in units of $k_{\rm F} = \sqrt{2m^*\mu_{\rm N}}/\hbar$) at phase difference $\phi = 0$ for three different values of the Zeeman field: (a) The spectrum is fully gapped at $B_\parallel = 0$. (b) At $B_\parallel = 0.21$ T, the gap at $k = 0$ closes. (c) At $B_\parallel = 0.3$ T, the gap at $k = 0$ has reopened, implying a topologically inverted superconducting gap. The gap at non-zero momentum remains non-zero throughout. (d) Andreev bound state spectrum of a finite-length planar Josephson junction ($l = 4\,\mu$m) with open boundary conditions. The closing and reopening of the superconducting gap at $B_\parallel = 0.21$ T is followed by the appearance of a Majorana state at zero energy (red), signaling a transition to the topological phase.

In the model, the quasi-one-dimensional junction supports Andreev bound states with momentum dispersion as shown in Fig. 3, where k is momentum parallel to the SN interfaces. At zero field [Fig. 3(a)], the spectrum shows a momentum-dependent superconducting gap that is induced by lateral proximity effect from the leads. At $B_\parallel \sim 0.2$ T a topological phase transition occurs, signaled by a closing of the gap at $k = 0$ [Fig. 3(b)]. Increasing $B_\parallel$ further reopens the gap, as illustrated in Fig. 3(c) for the case $B_\parallel = 0.3$ T. Notice that the spectrum remains gapped at finite $k \sim \pm k_{\rm F}$ throughout this field range. Correspondingly, in a Josephson junction with open boundary conditions, the bulk remains gapped away from the transition point. Figure 3(d) shows the model spectrum in a finite-length junction undergoing a gap closing at $B_\parallel \sim 0.2$ T and reopening, accompanied by the appearance of a zero-energy state. The zero-energy state observed in the model corresponds to a Majorana

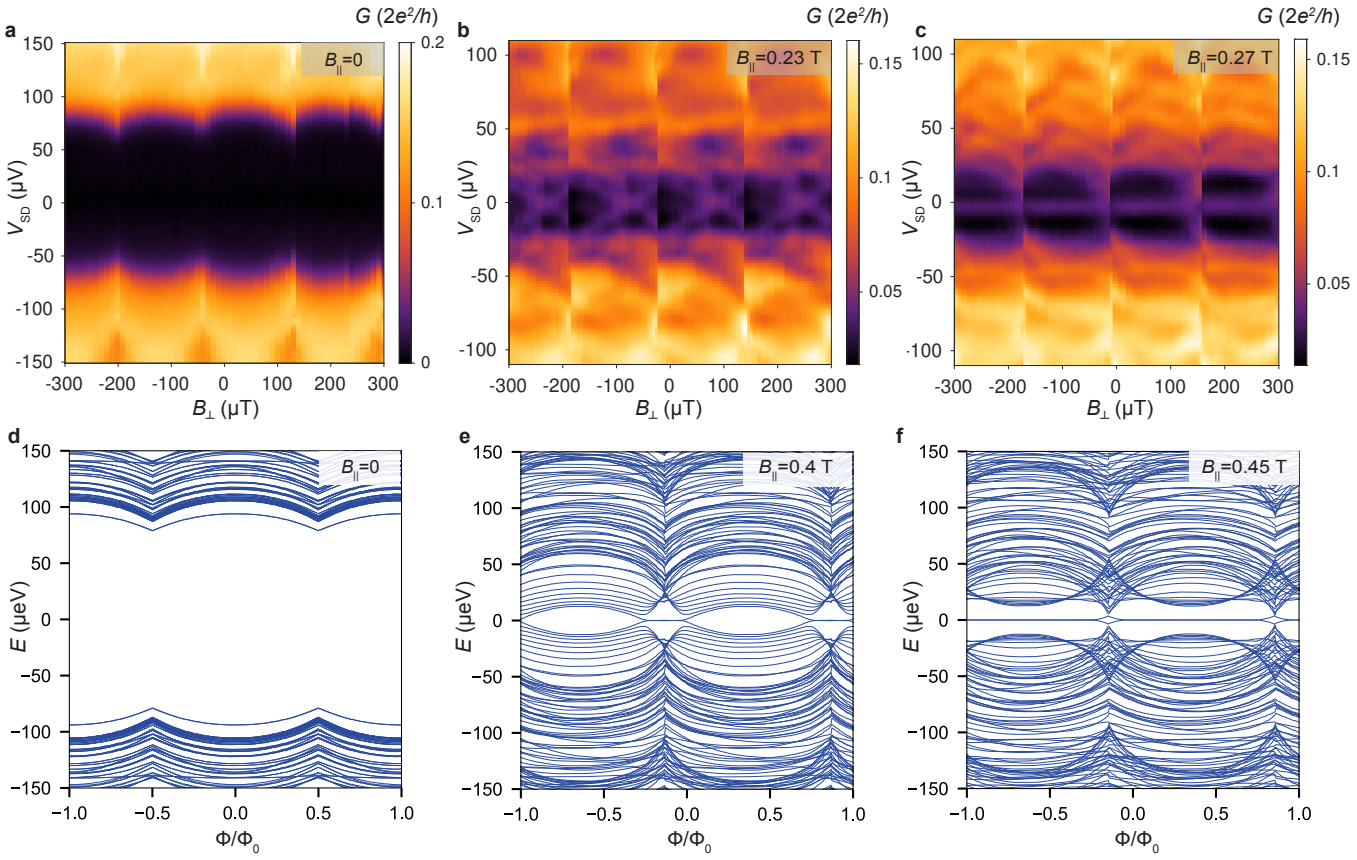

FIG. 4. **Flux dependence.** Differential conductance, G, as a function of source-drain bias $V_{\rm SD}$ and out-of-plane magnetic field $B_\perp$ penetrating the flux loop, at different values of in-plane magnetic field $B_\parallel$. (a) At $B_\parallel = 0$, the superconducting gap is modulated periodically as a function of $B_\perp$. The period corresponds to $\Phi_0 = h/2e$ through the superconducting loop. (b) At $B_\parallel = 0.2$ T, states cross zero energy in a bowtie shape, indicating a phase-dependent gap closing. (c) At $B_\parallel = 0.27$ T the superconducting gap reopens with a stable ZBCP. (d)–(f) Theoretical spectra as a function of the flux at three values of $B_\parallel = 0$, 0.4 T and 0.45 T (note, these are not the same fields as the experimental data in a-c, suggesting only qualitative correspondence). The simulations take into account the inductance $L = 2$ nH of the flux loop. This reduces the degree of phase modulation of the superconducting gap (see Methods).

zero mode.

B. Flux dependence

We next examine the effects of phase bias on subgap spectroscopy. Figures 4(a-c) show tunnelling spectra as a function of $B_\perp$ at different values of $B_\parallel$ in Device 1. At $B_\parallel = 0$ [Fig. 4(a)], the induced superconducting gap is modulated periodically as a function of $B_\perp$ with a periodicity of $\Delta B_\perp \sim 170$ μT, corresponding to one flux quantum $\Phi_0 = h/2e$ through the loop. The maximum (minimum) induced gap is $\Delta \sim 80$ μeV (50μeV) at integer (half-integer) flux through the loop. Around half flux quantum values, sharp switches are observed, which we attribute to phase jumps due to the large inductance of the loop, $L \sim 2$ nH [21] (see Methods).

Increasing $B_\parallel$ from zero, the phase-dependent states initially moved to lower energy up to the first gap closing. Figure 4(b) shows the phase-dependent spectrum at $B_\parallel = 0.23$ T, corresponding to the first gap closing in Fig. 2(a). Within each flux lobe, a bowtie-shaped set of states crossing zero energy was observed, creating a gapless spectrum. When the in-plane field was increased to $B_\parallel = 0.27$ T, the gap reappeared along with a ZBCP [Fig. 4(c)]. The ZBCP displays no observable dependence on $B_\perp$, while the gap shows strong phase dependence with the lowest-lying energy level at $E \sim 30$ μeV. In contrast to the phase-dependent spectrum at $B_\parallel = 0$ [Fig. 4(a)], spectra at finite parallel field [Figs. 4(b-c)] are asymmetric in phase bias within each lobe [2, 35–37].

The numerical bound-state spectrum was determined as a function of Φ, including the effect of loop inductance (see Methods). Figures 4(d-f) show numerical spectra with variation of the magnetic flux at three values of $B_\parallel$. At zero in-plane magnetic field [Fig. 4(d)], the spectrum is spin degenerate and all Andreev bound state energies are periodically modulated as a function of Φ. At inter-

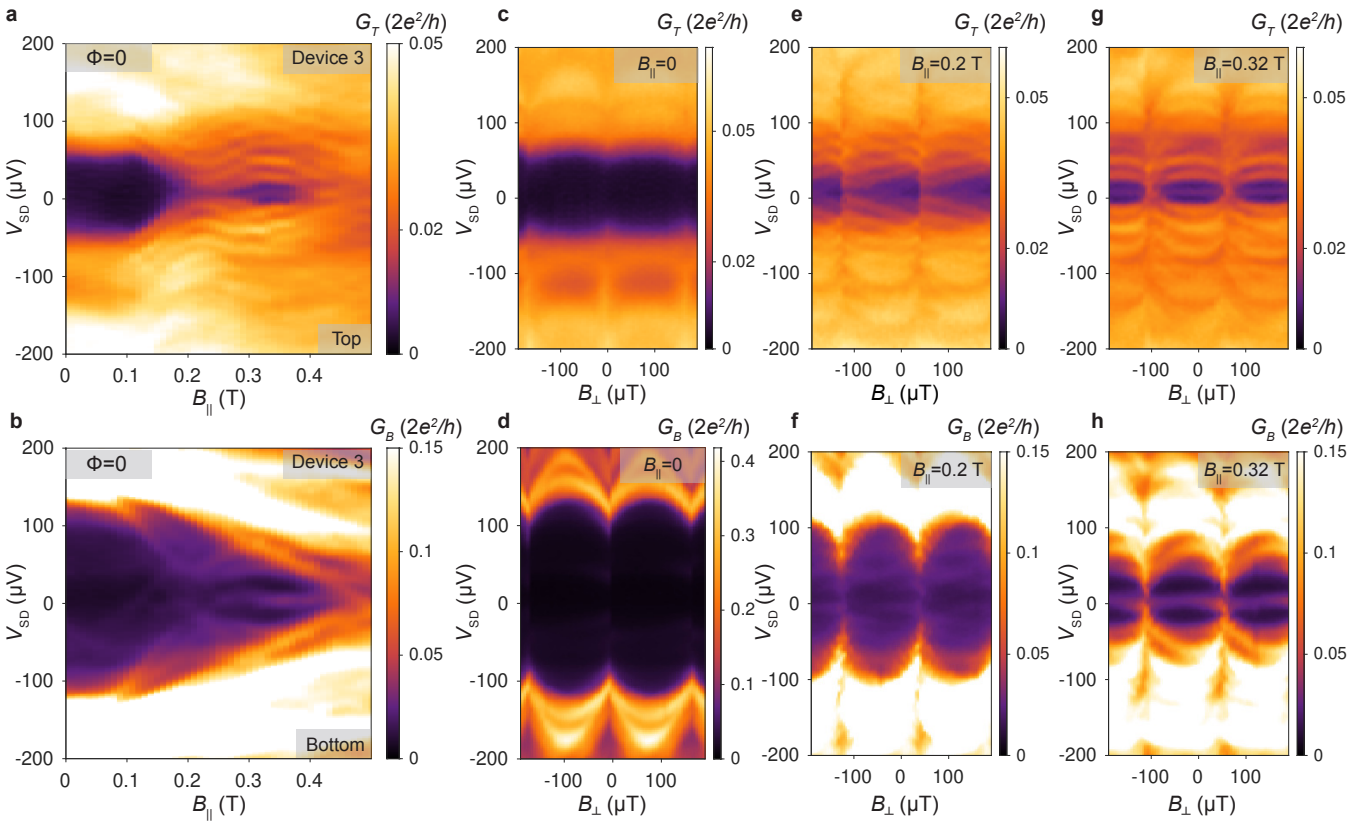

FIG. 5. **Two-ended tunnelling spectroscopy at the two ends of the junction.** Differential conductance measured as a function of source-drain bias $V_{\rm SD}$ and in-plane magnetic field $B_\parallel$ (a) G_T the top end and (b) G_B at the bottom end. The phase bias is set to $\Phi = 0$. Both ends display a closing and reopening of the gap at $B_\parallel$ ∼0.22 T followed by a zero-bias conductance peak. Simultaneous differential conductance measured at the top end and bottom end as a function of source-drain bias $V_{\rm SD}$ and out-of-plane magnetic field $B_\perp$ for different values of in-plane magnetic field $B_\parallel$. (c) and (d) At $B_\parallel = 0$, the superconducting gap is modulated periodically at both ends as a function of $B_\perp$ with the same periodicity and zero relative phase difference. (e) and (f) At $B_\parallel = 0.2$ T, the spectrum at both ends becomes gapless for all values of $B_\perp$. (g) and (h) At $B_\parallel = 0.3$ T the superconducting gap reopens with a stable zero-bias conductance peak at both ends of the device. Gate voltages were $V_1 = +189$ mV, $V_{\rm SC} = -2.6$ V, $V_{\rm qpc,top} = -6$ mV,$V_{\rm top} = -0.1$ V, $V_{\rm qpc,bot} = -265$ mV, $V_{\rm bot} = +0.2$ V, and $V_{\rm loop} = -3.0$ V.

mediate magnetic fields [Fig. 4(e)], the system is trivial in some range of Φ and topological in another range. In the topological region, a zero-energy state appears in the gap. These regions are separated by a gap-closing transition. For higher magnetic fields [Fig. 4(f)], the spectrum becomes topological for all values of Φ and the junction hosts a stable zero-energy state. The orbital effect from the in-plane magnetic field also induces a phase shift in the spectrum, such that the flux lobes are not symmetric about $\Phi = 0$ at non-zero values of $B_\parallel$.

We next examine the effect on the spectrum when $B_\parallel$ was tilted by small angles in the plane of the junction. As shown in Figs. S8 (a-c) [23], a tilt angle of $\sim 20^\circ$ closed the reopened gap. Similar behavior is seen in the model, though with greater sensitivity to tilt, as seen in Figs. S8 (d-f) [23].

C. Correlated gap-reopening in two-ended spectroscopy

Next, we investigate simultaneous tunnelling spectroscopy at both ends of the device using the two QPCs in Device 3. Differential conductances $G_{\rm T}$ and $G_{\rm B}$, measured at the top (top row of Fig. 5) and bottom (bottom row of Fig. 5) of the junction show correlated modulation of the superconducting gaps at the two ends as a function of $B_\perp$ with flux switches occurring at the same values of $B_\perp$ at both ends [Figs. 5(c) and 5(d)]. The sizes of the superconducting gaps at the two ends are different, with $\Delta_{\rm T} \sim 50$ μeV at the top and $\Delta_{\rm B} \sim 120$ μeV at the bottom. In the presence of an in-plane magnetic field, the gaps at the two ends disappeared simultaneously at $B_\parallel \sim 0.2$ T before reopening and undergoing a final gap closure at $B_\parallel \sim 0.48$ T. A gapless spectrum at $B_\parallel \sim 0.2$ T was seen for all values of $B_\perp$ [Figs. 5(e,f)]. At

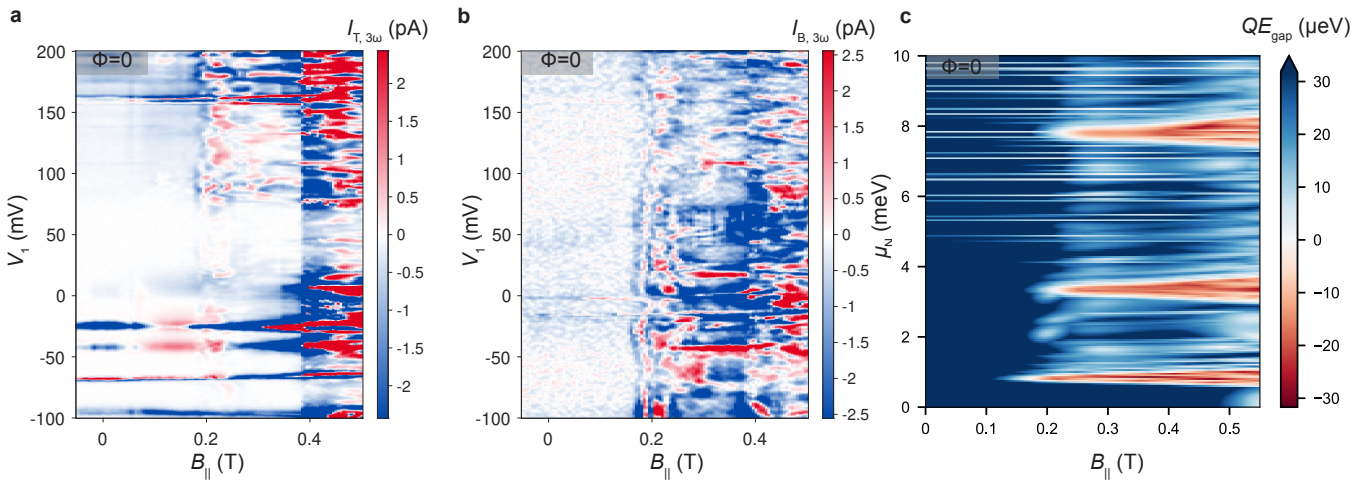

FIG. 6. **Two-ended third harmonic of the tunnelling current at the two ends.** Third-harmonic current measured at $V_{SD} = 0$ as a function of V_1 and in-plane magnetic field $B_\parallel$ (a) $I_{T,3\omega}$ at the top and (b) $I_{B,3\omega}$ at bottom of the junction, at phase bias $\Phi = 0$. A positive signal indicates a zero-bias conductance peak [9]. At $B_\parallel = 0.3$ T, we estimate the percentage of V_1 space that produces a positive third harmonic signal as $P_{Z,T} \sim 11\%$ at the top tunnel probe and $P_{Z,B} \sim 13\%$ at the bottom tunnel probe. (c) Theoretical topological phase diagram in the plane of the parallel magnetic field $B_\parallel$ and the chemical potential μ_N in the normal region (at $\phi = 0$). The colors indicate the topological invariant $\mathcal{Q}$, which is $+1$ (-1) for the trivial (topological) phase, multiplied by the energy gap. The diagram exhibits appreciable topological regions starting near $B_\parallel \sim 0.2$ T. The near-closings of the gap at $B_\parallel \sim 0.2$ T are almost independent of μ_N. These are not $k = 0$ gap closings and are thus not related to a class-D topological phase transition [33, 34].

$B_\parallel \sim 0.3$ T, the maximal reopened gaps at the two ends have different magnitudes, with a smaller gap at the top end ($\Delta_T \sim 30$ μeV) compared to the bottom end ($\Delta_B \sim 50$ μeV). Both ends display ZBCPs that emerge from the gap reopening and were reasonably stable for a range of in-plane magnetic field, phase [Figs. 5(g,h)], as well as junction gate voltage gate V_1. However, their range in V_1 was not strongly correlated (see Supplementary Material Fig. S9 [23]).

In Device 4, apart from measuring similar two-ended tunneling characteristics as Device 3 (see Fig. S10 [23]), we also measure the third-harmonic of the tunneling current simultaneously at both ends of the device at $V_{SD} = 0$, while sweeping V_1 and $B_\parallel$ continuously, to identify correlations between the two ends [Fig. 6(a),(b)]. A positive signal indicates a zero-bias conductance peak [9]. The first closing of the gap produces a region with intermittent positive third-harmonic current at $B_\parallel \sim 0.2$ T, reflecting a crossing of states through zero bias, appearing as a vertical feature that has weak dependence on V_1. This appears simultaneously at both ends, showing the end-to-end correlated nature of this feature, and its stability over the entire operable range of V_1 spanning 300 mV. At $B_\parallel > 0.4$ T, the third-harmonic current is positive for a sizable fraction of V_1, associated with a reclosing of the gap. For $0.2\ \text{T} \leq B_\parallel \leq 0.4$ T, regions of V_1 with positive third harmonic correspond to ZBCPs after the gap reopening.

This compares well with the theoretical model where the gap closure around $B_\parallel \sim 0.2$ T is robust, i.e., insensitive to small changes in chemical potential, as shown in Fig. 6(c). This feature appears as the vertical white stripe at $B_\parallel \sim 0.2$ T, reflecting a tendency for the gap to close roughly independent of the chemical potential. This feature reflects either a topological transition accompanied by a zero-energy state or a near-closing of the gap without a topological transition, depending on relatively small changes in chemical potential or other model parameters. This is shown in the field spectra evaluated at different values of the chemical potential [Figs. S3 (a)-(f) [23]]. Particularly, chemical potentials exist where the apparent gap closing is not associated with a zero-energy state [Fig. S3(f) [23]]. This is different from the Zeeman-effect driven topological transition in nanowires, where reopening of the gap follows a parabolic profile in $B_\parallel - \mu_N$ space, and near-closings of the gap are not expected.

D. Topological interpretation

These observations indicate that the closing and reopening of the gap was strongly correlated at the two ends. This provides support for the bulk character of the transition, and argues against spurious effects such as Andreev-dot physics that typically produce localized features only at one device end. Furthermore, the formation of ZBCPs is correlated with the gap-reopening feature, as evident from our investigation of the gap-reopening transition in the experimentally accessible Φ–$B_\parallel$ plane [Fig. S4 and Fig. S5 [23]]. To obtain the critical field, B_c, at which the gap closes and reopens, we track the bow-

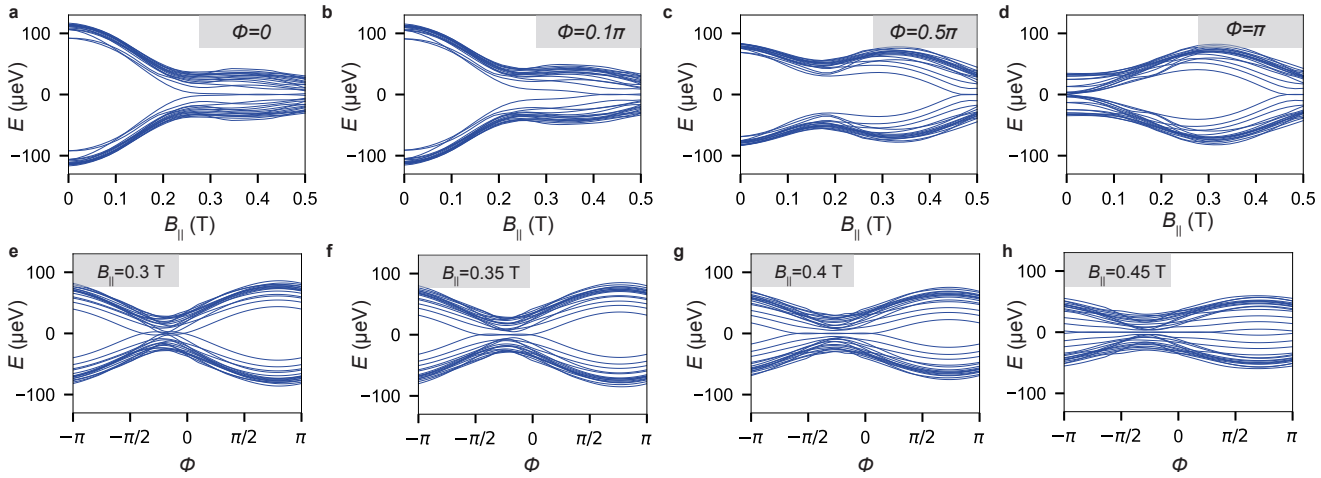

FIG. 7. **Numerics of quasi-Majoranas induced by a smooth potential.** The panels show the 30 lowest energy levels of the junction including a lounge-chair potential with parameters $f = 0.8$, $L_e = 1\,\mu$m, $L_p = 0.5\,\mu$m. The spectrum as a function of $B_\parallel$ at zero phase difference, shown in panel (a), has a feature resembling a gap reopening associated with the appearance of the zero-energy states, and therefore it could be confused with the behavior of a true Majorana zero mode. However, in the presence of a finite phase difference, the gap-reopening feature and the zero-energy state, both disappear, as shown in panels (b)-(d). (e)–(h) Spectra as a function of the phase difference for different in-plane fields, showing that the zero-energy states are not stable to phase variation. The phase behavior may therefore help distinguish between a quasi-Majorana state and a true Majorana zero mode.

tie shaped feature that appears in the phase-dependent spectra [Fig. S4 (b) [23]], representing gap closure. This feature evolves with both $B_\parallel$ and $B_\perp$ and can be tracked with an uncertainty of $\Delta B_\parallel \simeq 0.01$ T and $\Delta B_\perp \simeq 50\ \mu$T in Device 1 (see Fig. S13 [23]). In Device 2, the uncertainties are larger ($\Delta B_\parallel \simeq 0.03$ T and $\Delta B_\perp \simeq 50\ \mu$T, see Fig. S14 [23]). From this estimation, in Device 1 [Fig. S4 [23]], we obtain that the critical in-plane field required for gap reopening, $B_c = 0.19$ T at $\Phi = -\Phi_0/2$, and progressively increases to $B_c = 0.24$ T for $\Phi = +\Phi_0/2$. As the gap-reopening feature evolves, we observe that the ZBCP also evolves, and always follows the reopening of the gap, appearing when $B_\parallel$ exceeds B_c by about 0.01 – 0.03 T, for every value of Φ.

The formation of the ZBCP and the reopening of the gap appear to happen in concert, and are not independent events. The formation of non-topological zero-energy states is not generically expected to exhibit any correlation with a gap-reopening transition [38–42]. We also note that the formation of our ZBCPs is qualitatively different compared to nanowire geometries [6–8, 30, 43], where a pair of Andreev bound states emerges from the gap edge at $B_\parallel = 0$ and is lowered in energy with increasing magnetic field until the two states coalesce and stick at zero energy. In contrast, the ZBCPs discussed above emanate directly from the gap-reopening feature and their evolution from higher energy states cannot be discerned. These arguments favour a topological interpretation [42].

E. Non-topological interpretations

The absence of end-to-end ZBCP correlation at the two device ends is not consistent with clean topological superconductivity. This prompts us to consider non-topological interpretations of our data. Therefore, we numerically study the behavior of accidental zero-energy states that are formed due to chemical potential inhomogeneity [38, 44, 45]. Such zero-energy states, also known in the literature as quasi-Majorana states, have been previously investigated only in the nanowire geometry. As shown in Fig. 7(a), fine-tuned situations are possible where the system supports a stable zero-energy state associated with a gap-reopening-like feature. However, in our model, such zero-energy states were unstable to variations of phase bias [Fig. 7(b)-(d)] (also see Appendix F, and Fig. S16 [23]). This does not compare well with our experiments where both the gap-reopening and ZBCP were found to be robust against phase variations [Figs.4, S4 and S5 [23]]. On the other hand, when we deliberately tuned the device to host end-dots, the zero-bias Andreev states produced by them were not associated with a gap reopening, and were unstable to phase variations, as predicted by theory (see Fig. S17 [23]).

However, we cannot rule out other non-topological situations where behavior comparable to our experiment may be reproduced. Since the planar Josephson junction is a relatively new platform for topological superconductivity, we invite further theoretical discussions on this matter, highlighting that the phase degree of freedom may provide a discriminatory probe, absent in the

nanowire setup, that can help distinguish topological and non-topological zero-energy states.

IV. SUMMARY

We have presented a detailed investigation of planar Josephson junctions in the context of topological superconductivity. Prominently, the reopening of the gap together with the presence of zero-bias peaks, and the dependence of these features on phase bias and chemical potential are captured well by our theoretical model where orbital effects were found to be important for a topological superconducting state. Within a topological interpretation, the general lack of end-to-end correlations of ZBCPs suggests that disorder creates disjointed topological segments along the length of the junction. Combined with nonlocal conductance spectroscopy on the same devices, reported in a separate publication [46], we speculate that disorder strength in our systems is low enough to allow observation of a simultaneous reopening of the gap on the ends, but not so low yet as to observe an uninterrupted topological phase. Looking ahead, modest improvements in material quality may allow pristine topological superconductivity to emerge on this platform. Combined with recent developments in spatial manipulation of Andreev states using phase textures [47], a near-term fusion/braiding experiment appears within experimental reach [48].

Acknowledgements

We thank Geoff Gardener and Sergei Gronin for contributions to materials design and growth. We thank Andrey Antipov, Roman Lutchyn, Chetan Nayak, and Ivan Sadovskyy for useful discussions, in particular for pointing out the importance of orbital contributions in the model. We thank Karsten Flensberg, Antonio Fornieri, Raquel Queiroz, Noam Schiller, and Saulius Vaitiekėnas for insightful discussions. We acknowledge support from the Danish National Research Foundation, a research grant (Project 43951) from VILLUM FONDEN, the ERC under the Horizon 2020 Research and Innovation programme (LEGOTOP No. 788715 and HQMAT No. 817799), the DFG (CRC/Transregio 183, EI 519/7-1), the BSF and NSF (2018643), the ISF Quantum Science and Technology (2074/19), and a research grant from Irving and Cherna Moskowitz. H.R.W. and M.R.L. thank the Weizmann Institute of Science for hospitality via the Yutchun Program during the initial phase of the work.

Data Availability

Numerical data for all figures, additional data for 10 SNS devices and the Hall bar device, code for the theoretical analysis, and a plotting program for the data are available at https://doi.org/10.5281/zenodo.5831419.

Appendix A: Wafer structure

The wafer structure used in this work consists of an InAs two-dimensional quantum well in epitaxial contact with Al. The wafer was grown on an insulating InP substrate by molecular beam epitaxy comprising a 100-nm-thick $In_{0.52}Al_{0.48}As$ matched buffer, a 1 μm thick step-graded buffer realized with alloy steps from $In_{0.52}Al_{0.48}As$ to $In_{0.89}Al_{0.11}As$ (20 steps, 50 nm/step),a 58 nm $In_{0.82}Al_{0.18}As$ layer, a 4 nm $In_{0.75}Ga_{0.25}As$ bottom barrier, a 7 nm InAs quantum well, a 10 nm $In_{0.75}Ga_{0.25}As$ top barrier, two monolayers of GaAs and a 7 nm film of epitaxially grown Al. The top Al layer was grown in the same molecular beam epitaxy chamber used for the rest of the growth, without breaking the vacuum.

Hall effect measurements were performed in Hall bar devices with Al etched away (see Fig. S12 for Hall effect measurements [23]). The Hall bar was covered with the same dielectric material as used in the Josephson junction experiments, grown under nominally identical conditions and of the same thickness. A peak electron mobility $\mu = 43,000$ cm^2/Vs was observed at a carrier density of $n = 8 \times 10^{11}$ cm^{-2}, corresponding to a peak mean free path of $l_e \sim 600$ nm at top gate voltage $V_{\mathrm{TG}} = -0.8$ V. In the junction experiments, we typically use $V_{\mathrm{sc}} = -3$ V to control density under the superconducting leads and $V_1 = 0 - 0.1$ V to control density in the barrier region. Different geometries and lateral gate coupling makes it difficult to compare these voltages directly. To get a rough idea, however, taking l_e to be around 600 nm in the junction yields quasi-ballistic motion along the junction, $l \sim 3l_e$, and ballistic motion across the junction, $w_n \sim l_e/6$.

Transport characterization of a large-area Hall bar with Al in place yielded a critical field of 2.5 T [9, 49] for the parent Al layer, considerably larger than field where the gap closure occurs, ~ 0.5 T.

Appendix B: Device fabrication

Devices were fabricated using conventional electron beam lithography. Devices on the same chip were electrically isolated from each other using a self-aligned mesa etch process, first by removing Al using Transene D wet etch, followed by a wet etch in H_2O:$C_6H_8O_7$:H_3PO_4:H_2O_2 (220:55:3:3) to remove the semiconductor to a depth of $\sim$ 300 nm. Next, Al was selectively removed leaving the Josephson junction and flux loop. A 15 nm thick layer of HfO_2 grown at 90°C using atomic layer deposition (ALD) was used as the gate dielectric. Gates were defined using electron beam lithography followed by e-beam evaporation of Ti/Au layers of thicknesses (5 nm/20 nm) for finer structures and (5 nm/350 nm) for the bonding pads. The bottom Ti/Au ohmic contact (5 nm/350 nm) was formed by etching away a U-shaped trench in the mesa and then contacting the InAs 2DEG. No additional surface preparation was

used. An additional HfO_2 layer deposited by ALD and subsequent lift-off was used to isolate the Ti/Au ohmic from the superconducting loop and mesa.

Appendix C: Electrical transport measurements

Electrical transport measurements were performed in an Oxford Triton dilution refrigerator at a base temperature of 20 mK using conventional low-frequency AC lock-in techniques at 31.5 Hz excitation frequency, an AC excitation amplitude of 3 μV and a variable DC voltage V_{SD} for bias spectroscopy. The current through the device was recorded using a low-impedance current-to-voltage converter that was attached to the ohmic contact connected to the superconducting loop. For measuring the third harmonic of the current, a higher AC excitation amplitude of 10 μV was used. Magnetic field to the sample was applied using a three-axis (B_x, B_y, B_z)=(1T, 1T, 6T) vector magnet.

We fabricated 32 devices, of which 10 were measured. We summarize the behavior of these devices. We also estimate the probability $P_{\mathrm{Z,T(B)}}$, of observing a ZBCP, which is defined as the percentage of operable V_1 gate space that shows stable ZBCPs at the top (bottom) end.

Device 1: Gap reopening with ZBCP at top end, bottom QPC did not work. $P_{\mathrm{Z,T}} \sim 15\%$.

Device 2: Gap reopening at both ends, ZBCP only at the top end. $P_{\mathrm{Z,T}} \sim 30\%$.

Device 3: Gap reopening and stable ZBCP at both ends. $P_{\mathrm{Z,T}} \sim 10\%$, $P_{\mathrm{Z,B}} \sim 5\%$.

Device 4: Gap reopening and stable ZBCP at both ends. $P_{\mathrm{Z,T}} \sim 10\%$, $P_{\mathrm{Z,B}} \sim 10\%$.

Device 5: Gap reopening and stable ZBCP at both ends. $P_{\mathrm{Z,T}} \sim 5\%$, $P_{\mathrm{Z,B}} \sim 5\%$.

Device 6: Gap reopening at both ends. Stable ZBCP at top end. ZBCP at bottom end oscillated as a function of in-plane magnetic field. $P_{\mathrm{Z,T}} \sim 5\%$, $P_{\mathrm{Z,B}} \sim 5\%$.

Device 7: Gap reopening on both ends. Soft gap at low fields at both ends.

Device 8: Spectroscopy possible at both ends, however induced superconducting gap at the bottom end collapsed at $B_{\parallel} \sim 150$ mT.

Device 9: Spectroscopy not possible at bottom end.

Device 10: No detectable superconducting gap on either end.

Theoretical simulation: $P_{\mathrm{Z,T}} = P_{\mathrm{Z,B}} \sim 9$–$18\%$.

Appendix D: Magnetic field alignment

The sample is oriented with respect to the vector magnet such that B_x of the magnet is nominally along $B_{\perp}$, the field in the direction perpendicular to the plane of the wafer [Fig. 1(c)] and B_z of the magnet is nominally parallel to $B_{\parallel}$ the field direction along the SN interfaces [Fig. 1(c)]. However, sample misalignment causes the magnet B_z to have a small contribution to $B_{\perp}$, which controls the flux through the superconducting loop. At non-zero B_z, it is therefore necessary to identify the proportional amount of B_x that results in constant flux through the loop. At zero B_z, the value of B_x at which the superconducting gap is maximised corresponds to zero and multiples of Φ_0, while distinct phase jumps appear at odd multiples of $\Phi_0/2$. This allows us to calibrate the flux through the device at zero B_z. At finite B_z, the superconducting gap acquires a phase-asymmetric dispersion, and the maxima of the gap cannot be used to track lines of constant flux. Instead, we use the phase jumps to identify lines of constant flux through the device. This allows us to define magnetic fields $B_{\parallel}$ and $B_{\perp}$ that compensate for the finite tilt of the sample.

Appendix E: Estimation of flux loop inductance

The inductance of the superconducting loop is a combination of the geometric inductance and the kinetic inductance of the thin Al layer, and is dominated by the latter [21]. We estimate the geometric inductance of the loop as $L_G \sim 2.5$ pH. The kinetic inductance of a thin superconductor is proportional to its sheet resistivity and is given as

$$L_K = \frac{l_s}{w_s}\frac{h}{2\pi^2 e}\frac{R_{\square}}{\Delta}, \tag{E1}$$

where l_s and w_s are the length and width of the superconducting stripe defining the superconducting loop including the meanders that are part of the superconducting leads, and $R_{\square}$ is the normal-state sheet resistivity of the Al/InAs layer. $l_s/w_s \sim 240$ in our device and has two contributions, $l_1/w_1 \sim 40$ for the U-shaped part of the loop and $l_2/w_2 \sim 200$ arising from the meandering part of the superconducting leads. The sheet resistance $R_{\square}$ in our material is measured as $\sim$6 Ω in the normal state of a large area Al Hall bar [49] and the superconducting gap $\Delta \sim 200$ μeV. This leads to a kinetic inductance $L_K \sim 1.5$ nH, and total inductance $L \sim L_K \sim 1.5$ nH. In our numerical simulations of the flux dependence of Andreev bound state spectrum, we find that $L \sim 2$ nH qualitatively reproduces the features observed in the measured subgap spectra (see Fig. 4).

Appendix F: Model

To model our device, we use an extension of the Hamiltonian proposed in Refs. [1, 2] to account for finite thickness and include orbital effects. The model is based on two layers of a two-dimensional semiconductor with Rashba spin-orbit coupling. We consider a rectangular device, with the rectangle divided into three parts by width: normal region in the middle with width w_n, and superconducting regions on two sides, each of width w. In the Nambu basis $(\psi_{\uparrow}, \psi_{\downarrow}, \psi_{\downarrow}^{\dagger}, -\psi_{\uparrow}^{\dagger})$, the Bogoliubov–de Gennes Hamiltonian is given by:

$$H = \left[-\frac{\partial_x^2 + \partial_y^2}{2m^*} - t_\perp \nu_x - \mu(y) + i\alpha(z)\left(\partial_x \sigma_y - \partial_y \sigma_x\right) \right] \tau_z + \frac{g(y)\mu_B B_\parallel}{2}\sigma_x + \Delta(y,z)\tau^+ + \Delta^*(y,z)\tau^-, \tag{F1}$$

where σ, τ, ν are Pauli matrices acting in spin, electron-hole, and layer basis, respectively. Here m^* is the effective mass of electrons in the semiconductor, $\alpha(z)$ is the layer-dependent Rashba spin-orbit coupling strength, $t_\perp$ is the inter-layer hopping amplitude, $B_\parallel$ is the magnetic field applied along the junction, and μ_B is the Bohr magneton. The g-factor $g(y)$ is different for the normal and superconducting regions, such that

$$g(y) = \begin{cases} g_N & |y| < \frac{w_n}{2} \\ g_S & \frac{w_n}{2} < |y| < w + \frac{w_n}{2}. \end{cases} \tag{F2}$$

Similarly, the chemical potential μ takes the values μ_N in the normal region and μ_S in the superconducting region. In the last two terms, $\Delta(y)$ is the superconducting pairing potential which is non-zero only in the superconducting region:

$$\Delta(y) = \begin{cases} 0 & |y| < \frac{w_n}{2} \\ \Delta e^{i\phi/2} & \frac{w_n}{2} < y < w + \frac{w_n}{2} \\ \Delta e^{-i\phi/2} & -w - \frac{w_n}{2} < y < -\frac{w_n}{2}. \end{cases} \tag{F3}$$

To model the finite thickness of the system, thereby accounting for the orbital effects of the in-plane magnetic field, we utilize the two-layer structure. Hopping between the two layers is described by the amplitude $t_\perp$. The orbital effect enters as a vector potential $\vec{A} = B_\parallel y \hat{z}$, where z is the out-of-plane direction; the vector potential is incorporated into the tight-binding Hamiltonian as a complex amplitude with the Peierls substitution [31]. Furthermore, the parallel magnetic field induces linear phase growth along the junction's cross section [28], which is modeled as an additional modulation $\propto B_\parallel yz$ to the superconducting phase. We note that another possibility of modeling the phase evolution is assuming the proximity effect is only present at the top layer and calibrating Δ accordingly. The basis of this approach is integrating out the proximitizing superconductor's degrees of freedom, and it yields very similar results to the ones we report here. In reality a detailed simulation of the system is more involved. It should include the effect of disorder in the Al and InAs layers, and consider a well with finite thickness in the z direction. We should therefore treat the Hamiltonian introduced in Eq. (F1) as a phenomenological model that, with a proper choice of effective parameters, reproduces qualitatively the experimental observations.

For our numerical calculations, we discretize the Hamiltonian to a tight-binding model on a square lattice of spacing $a = 10$ nm. Simulations are performed with the following parameters: $m^* = 0.026\, m_e$, $\Delta = 140$ μeV, $t_\perp = 10$ meV, $l = 4$ μm, $w_n = 100$ nm, $w = 200$ nm, $w_z = 10$ nm, $\mu_{SC} = 3.6$ meV, $\mu_N = 3.3$ meV. The g-factors are taken to be $g_N = 8$ and $g_S = 4$. We use the leads spectroscopy measurements [Fig. S2 [23]] to match A_{eff} (the effective cross section for the field-induced superconducting phase gradient), μ_{SC}, and the difference in spin-orbit coupling between the two layers. We obtained $A_{\text{eff}} = 0.4(2w + w_n)w_z$, $\mu_{SC} = 3.6$ meV, and the spin-orbit coupling constants $\alpha(0) = 15$ meV nm, $\alpha(1) = -\alpha(0)/4$. Pfaffians were computed using the pfpack software package [50]. Some of the preliminary simulations were performed using the Kwant software package [51].

We further introduce the effect of finite loop inductance to simulate the flux jumps observed in the experimental phase spectra by establishing the relation between the external flux (Φ) penetrating the device and the phase difference (ϕ) dropped across the Josephson junction. The spectra of the system obtained as a function of ϕ can then be mapped to spectra as a function of the applied flux Φ. Given a phase difference ϕ, we calculate the ground-state energy $E_{GS}(\phi)$ by summing up the energies of all occupied levels $E < 0$. We then calculate the supercurrent at zero temperature, $I(\phi) = -\frac{dE_{GS}}{d\phi}$. In the presence of a finite loop inductance L, the external flux Φ and the phase difference across the Josephson junction ϕ are related as $\Phi = (\Phi_0/2\pi)\phi - LI(\phi)$, where the second term accounts for the magnetic flux dropped across the flux loop when a supercurrent $I(\phi)$ flows through it. For each Φ, several values of ϕ may be possible. We use a quasi-static approximation and choose the value of ϕ that minimises the total energy $E_{tot}(\phi) = E_{GS}(\phi) + \frac{1}{2}LI^2(\phi)$, where the second term is the magnetic energy stored in the loop. Once the mapping $\Phi \to \phi$ is established, we obtain the energy spectrum as a function of Φ. Here we provide simulations with $L = 2$ nH.

As a consequence of this effect, the observed phase modulation of Andreev bound states is reduced as shown in Fig. 4(d)-(f). Since a portion of the applied magnetic flux drops across the loop inductance, the flux dropped across the SNS junction is reduced, especially close to $\phi \simeq \pi$, where the current through the junction, and therefore the flux dropped on the loop inductance $LI(\phi)$ is maximum. Additionally, we note that in conventional radio-frequency SQUIDs, loop inductance may lead to hysteretic operation of the device where the flux across the junction changes hysteretically depending on the sweep direction of the external magnetic field that controls the applied flux [52, 53]. In our experiments, we did not observe any hysteretic behavior, suggesting that the system chooses to minimize its ground state energy for every value of applied $B_\perp$. This is possible since $B_\perp$ is swept very slowly in our experiments (10 μT for every sweep of the source-drain bias voltage, which takes about 20s, giving an effective sweep rate of 0.5 μT/s). The system is therefore allowed enough time to find the ground-state energy minimum which typically scales as the inverse of the Josephson energy. Similar reduction in

phase modulation of Andreev bound states was recently observed in [54] and also attributed to the loop inductance.

Appendix G: Numeric analysis of disorder and non-topological zero-energy states

In addition, we examined the effect of disorder by introducing a random potential term $V(x,y)$ into the Hamiltonian. We took $V(x,y)$ to be a random uncorrelated Gaussian variable, $\langle V(x,y)V(x',y')\rangle = V_0^2\delta(x-x')\delta(y-y')$. The corresponding tight-binding version of this random potential is a site-dependent random addition to the chemical potential, whose variance $V_{\rm TB}$ is related to the continuum value V_0 by $V_{\rm TB}^2a^2 = V_0^2 = \frac{1}{m^*\tau} = \frac{2a^2t_\parallel}{\tau}$, where τ is the transport lifetime. Therefore, $V_{\rm TB}^2 = 2t_\parallel/\tau$. We took $\hbar/\tau = 1\,\text{meV}$ in the region not covered by the superconductor and $\hbar/\tau = 0.5\,\text{meV}$ for the covered region (due to the lower Fermi velocity there). For this intermediate range of τ, roughly consistent with the mean free path from Fig. S12 [23], disorder may or may not destroy the zero-energy state, depending on the particular disorder realization. When τ is increased by a factor of 10 (weak disorder) the zero-energy state is almost always observed, while decreasing τ by a factor of 10 (strong disorder) essentially eliminates the zero-energy state.

We also explored additional explanations for our data which rely on topologically trivial mechanisms for the emergence of zero-energy states. Such Andreev bound states, sometimes termed quasi-Majorana states, may emerge when the confining potential is smooth near the edges of the system [38, 42, 44, 45]. To investigate this possibility, we added a modulation to the chemical potential in both normal and superconducting parts of the junction, according to

$$\mu_{\rm N}(x) = \mu_{\rm N,0}F(x),\ \mu_{\rm SC}(x) = \mu_{\rm SC,0}F(x),$$
$$F(x) = f + \frac{1-f}{2}\left[1+\tanh\left(\frac{x-L_e}{L_p}\right)\right]. \qquad \text{(G1)}$$

The modulation function $F(x)$ is the so-called lounge-chair potential: it curves smoothly near the edge of the junction and takes on a constant value in the bulk. It is parametrized by f (the offset at the edge), L_e (the penetration of the potential into the junction), and L_p (the smoothness of the potential). The parameter profiles with this modulation are shown in Fig. S15 [23]. By varying f, L_e, L_p and changing the chemical potential $\mu_{\rm N,0}$, we were able to find several examples of spectra where near-zero-energy states appear due to this smooth potential, in a region of parameter space that does not support a topological phase. Such examples are shown in Figs. 7, S16[23]. These states are stable to the in-plane field, but they are very unstable to variations in the superconducting phase difference ϕ. This should be contrasted with true Majorana zero modes which, in at least in some regions of parameter space, can be robust to phase difference. We therefore suggest that the phase stability is a powerful tool for differentiating between trivial Andreev bound states and Majorana zero modes in planar Josephson junctions, unlike nanowires where this degree of freedom is not available.

We suggest that the difference between the ubiquity of quasi-Majoranas in nanowires and their relative rarity in our setup originates from the fundamental difference between the two systems. In nanowires, or in Josephson junctions with narrow superconductors, topological transitions are induced by tuning the Fermi energy and the parallel field. When the Fermi energy varies slowly close to the wire's ends, this variation induces a series of points where the wire transitions between topological and trivial states, and each such point comes with a localized zero mode. In contrast, in a junction made of semi-infinite superconductors, topological transitions are tuned by varying the phase difference and the parallel field, with a weak dependence on the Fermi energy. Thus, the variation of the Fermi energy close to the junction's end does not lead to such a series of transitions. The junction we study here is at the intermediate limit, with a relatively weak dependence of the phase diagram on the Fermi energy, and hence the relative rarity of the quasi-Majoranas in our numerical studies.

[1] M. Hell, M. Leijnse, and K. Flensberg, Phys. Rev. Lett. **118**, 107701 (2017).
[2] F. Pientka, A. Keselman, E. Berg, A. Yacoby, A. Stern, and B. I. Halperin, Phys. Rev. X **7**, 021032 (2017).
[3] F. Setiawan, A. Stern, and E. Berg, Phys. Rev. B **99**, 220506 (2019).
[4] Y. Oreg, G. Refael, and F. von Oppen, Phys. Rev. Lett. **105**, 177002 (2010).
[5] R. M. Lutchyn, J. D. Sau, and S. Das Sarma, Phys. Rev. Lett. **105**, 077001 (2010).
[6] V. Mourik, K. Zuo, S. M. Frolov, S. R. Plissard, E. P. A. M. Bakkers, and L. P. Kouwenhoven, Science **336**, 1003 (2012).
[7] A. Das, Y. Ronen, Y. Most, Y. Oreg, M. Heiblum, and H. Shtrikman, Nature Physics **8**, 887 (2012).
[8] M. Deng, S. Vaitiekėnas, E. B. Hansen, J. Danon, M. Leijnse, K. Flensberg, J. Nygård, P. Krogstrup, and C. M. Marcus, Science **354**, 1557 (2016).
[9] A. Fornieri, A. M. Whiticar, F. Setiawan, E. Portolés, A. C. Drachmann, A. Keselman, S. Gronin, C. Thomas, T. Wang, R. Kallaher, *et al.*, Nature **569**, 89 (2019).
[10] M. C. Dartiailh, W. Mayer, J. Yuan, K. S. Wickramasinghe, A. Matos-Abiague, I. Žutić, and J. Shabani, Phys. Rev. Lett. **126**, 036802 (2021).
[11] H. Ren, F. Pientka, S. Hart, A. T. Pierce, M. Kosowsky, L. Lunczer, R. Schlereth, B. Scharf, E. M. Hankiewicz, L. W. Molenkamp, *et al.*, Nature **569**, 93 (2019).
[12] C. T. Ke, C. M. Moehle, F. K. de Vries, C. Thomas,

S. Metti, C. R. Guinn, R. Kallaher, M. Lodari, G. Scappucci, T. Wang, *et al.*, Nature communications **10**, 1 (2019).
[13] B. Nijholt and A. R. Akhmerov, Phys. Rev. B **93**, 235434 (2016).
[14] G. W. Winkler, D. Varjas, R. Skolasinski, A. A. Soluyanov, M. Troyer, and M. Wimmer, Phys. Rev. Lett. **119**, 037701 (2017).
[15] G. W. Winkler, A. E. Antipov, B. van Heck, A. A. Soluyanov, L. I. Glazman, M. Wimmer, and R. M. Lutchyn, Phys. Rev. B **99**, 245408 (2019).
[16] O. Lesser, K. Flensberg, F. von Oppen, and Y. Oreg, Phys. Rev. B **103**, L121116 (2021).
[17] O. Lesser, A. Saydjari, M. Wesson, A. Yacoby, and Y. Oreg, Proceedings of the National Academy of Sciences **118**, e2107377118 (2021).
[18] J. Shabani, M. Kjaergaard, H. J. Suominen, Y. Kim, F. Nichele, K. Pakrouski, T. Stankevic, R. M. Lutchyn, P. Krogstrup, R. Feidenhans'l, S. Kraemer, C. Nayak, M. Troyer, C. M. Marcus, and C. J. Palmstrøm, Phys. Rev. B **93**, 155402 (2016).
[19] W. S. Cole, S. Das Sarma, and T. D. Stanescu, Phys. Rev. B **92**, 174511 (2015).
[20] M. Kjærgaard, F. Nichele, H. Suominen, M. Nowak, M. Wimmer, A. Akhmerov, J. Folk, K. Flensberg, J. Shabani, w. C. Palmstrøm, *et al.*, Nature communications **7**, 1 (2016).
[21] F. Nichele, E. Portolés, A. Fornieri, A. M. Whiticar, A. C. C. Drachmann, S. Gronin, T. Wang, G. C. Gardner, C. Thomas, A. T. Hatke, M. J. Manfra, and C. M. Marcus, Phys. Rev. Lett. **124**, 226801 (2020).
[22] M. Kjaergaard, H. J. Suominen, M. P. Nowak, A. R. Akhmerov, J. Shabani, C. J. Palmstrøm, F. Nichele, and C. M. Marcus, Phys. Rev. Applied **7**, 034029 (2017).
[23] See Supplemental Material at URL which includes Refs. 55 and 56.
[24] T. Laeven, B. Nijholt, M. Wimmer, and A. R. Akhmerov, Physical Review Letters **125**, 086802 (2020).
[25] P. P. Paudel, T. Cole, B. D. Woods, and T. D. Stanescu, Phys. Rev. B **104**, 155428 (2021).
[26] W. McMillan, Physical Review **175**, 537 (1968).
[27] B. Aminov, A. Golubov, and M. Y. Kupriyanov, Physical Review B **53**, 365 (1996).
[28] M. Tinkham, *Introduction to Superconductivity*, 2nd ed., International Series in Pure and Applied Physics (McGraw-Hill, New York, 1996).
[29] J. Lee, B. Shojaei, M. Pendharkar, A. McFadden, Y. Kim, H. Suominen, M. Kjærgaard, H. Zhang, F. Nichele, C. Marcus, and C. Palmstrøm, Nano Letters **19**, 3083 (2019).
[30] F. Nichele, A. C. C. Drachmann, A. M. Whiticar, E. C. T. O'Farrell, H. J. Suominen, A. Fornieri, T. Wang, G. C. Gardner, C. Thomas, A. T. Hatke, P. Krogstrup, M. J. Manfra, K. Flensberg, and C. M. Marcus, Phys. Rev. Lett. **119**, 136803 (2017).
[31] R. Peierls, Zeitschrift für Physik **80**, 763 (1933).
[32] K.-H. Bennemann and J. B. Ketterson, *Superconductivity: Volume 1: Conventional and Unconventional Superconductors Volume 2: Novel Superconductors* (Springer Science & Business Media, 2008).
[33] A. Altland and M. R. Zirnbauer, Phys. Rev. B **55**, 1142 (1997).
[34] A. P. Schnyder, S. Ryu, A. Furusaki, and A. W. W. Ludwig, Phys. Rev. B **78**, 195125 (2008).
[35] A. A. Reynoso, G. Usaj, C. A. Balseiro, D. Feinberg, and M. Avignon, Phys. Rev. B **86**, 214519 (2012).
[36] T. Yokoyama, M. Eto, and Y. V. Nazarov, Phys. Rev. B **89**, 195407 (2014).
[37] L. Tosi, C. Metzger, M. F. Goffman, C. Urbina, H. Pothier, S. Park, A. L. Yeyati, J. Nygård, and P. Krogstrup, Phys. Rev. X **9**, 011010 (2019).
[38] G. Kells, D. Meidan, and P. W. Brouwer, Phys. Rev. B **86**, 100503 (2012).
[39] E. Prada, P. San-Jose, and R. Aguado, Phys. Rev. B **86**, 180503 (2012).
[40] C.-X. Liu, J. D. Sau, T. D. Stanescu, and S. Das Sarma, Phys. Rev. B **96**, 075161 (2017).
[41] H. Pan, W. S. Cole, J. D. Sau, and S. Das Sarma, Phys. Rev. B **101**, 024506 (2020).
[42] H. Pan and S. Das Sarma, Phys. Rev. Research **2**, 013377 (2020).
[43] H. J. Suominen, M. Kjaergaard, A. R. Hamilton, J. Shabani, C. J. Palmstrøm, C. M. Marcus, and F. Nichele, Phys. Rev. Lett. **119**, 176805 (2017).
[44] A. Vuik, B. Nijholt, A. Akhmerov, and M. Wimmer, SciPost Physics **7**, 061 (2019).
[45] R. Hess, H. F. Legg, D. Loss, and J. Klinovaja, Physical Review B **104**, 075405 (2021).
[46] A. Banerjee, O. Lesser, M. A. Rahman, C. Thomas, T. Wang, M. J. Manfra, E. Berg, Y. Oreg, A. Stern, and C. M. Marcus, Phys. Rev. Lett. **130**, 096202 (2023).
[47] A. Banerjee, M. Geier, M. A. Rahman, D. S. Sanchez, C. Thomas, T. Wang, M. J. Manfra, K. Flensberg, and C. M. Marcus, Phys. Rev. Lett. **130**, 116203 (2023).
[48] A. Stern and E. Berg, Phys. Rev. Lett. **122**, 107701 (2019).
[49] A. C. C. Drachmann, R. E. Diaz, C. Thomas, H. J. Suominen, A. M. Whiticar, A. Fornieri, S. Gronin, T. Wang, G. C. Gardner, A. R. Hamilton, F. Nichele, M. J. Manfra, and C. M. Marcus, Phys. Rev. Materials **5**, 013805 (2021).
[50] M. Wimmer, ACM Transactions on Mathematical Software **38**, 30:1 (2012).
[51] C. W. Groth, M. Wimmer, A. R. Akhmerov, and X. Waintal, New Journal of Physics **16**, 063065 (2014).
[52] C. Guarcello, R. Citro, O. Durante, F. S. Bergeret, A. Iorio, C. Sanz-Fernández, E. Strambini, F. Giazotto, and A. Braggio, Physical Review Research **2**, 023165 (2020).
[53] C. Guarcello, P. Solinas, M. Di Ventra, and F. Giazotto, Physical Review Applied **7**, 044021 (2017).
[54] C. M. Moehle, P. K. Rout, N. A. Jainandunsing, D. Kuiri, C. T. Ke, D. Xiao, C. Thomas, M. J. Manfra, M. P. Nowak, and S. Goswami, arXiv preprint arXiv:2207.06933 (2022).
[55] C. Beenakker, in *Quantum Dots: a Doorway to Nanoscale Physics* (Springer, 2005) pp. 131–174.
[56] S. Das Sarma, J. D. Sau, and T. D. Stanescu, Phys. Rev. B **86**, 220506 (2012).